Engineering Dirac cones and topological flat bands with organic molecules

Yoshiaki Shuku [1], Rie Suizu [1,2] Saya Nakano,[3] Masahisa Tsuchiizu,[3] and Kunio Awaga [1,*]

[1]*Department of Chemistry & Integrated Research Consortium on Chemical Sciences (IRCCS), Nagoya University, Furo-cho, Chikusa-ku, Nagoya 464-8602, Japan*

[2]*Japan Science and Technology Agency (JST), PRESTO, 4-1-8 Honcho, Kawaguchi, Saitama 332-0012, Japan*

[3]*Department of Physics, Nara Women's University, Kitauoyanishi-machi, Nara 630-8506, Japan*

We investigated polyhedral π-conjugated molecules with threefold rotation symmetry, which can be suitable building blocks for both Dirac cones and a topological flat-band system. The two dimensional network structures of such molecules can be characterized by intra- and intermolecular interactions. We constructed tight binding models of these structures by systematically changing the intra- (t_0) and intermolecular (t_1) transfer integrals as independent parameters. The degree of freedom for the interactions provides a topological flat band and a massless or massive Dirac cone. We analyzed the topological features and origins of the flat band and Dirac cone of a molecule-based triangular lattice.

I. INTRODUCTION

In the field of materials science, band theory provides a fundamental idea of how electrons behave and is used extensively to understand, explain, and predict solid-state physics. Electronic structures of graphene and related materials have attracted much attention over the years because of their unique electronic band structures and exotic physical properties [1–3]. Unique properties of graphene are discussed in terms of linear energy dispersions called Dirac cones, which give massless fermions [4]. Emerging beyond graphene, two-dimensional (2D) materials [5–7] such as transition metal dichalcogenides [8,9], transition metal carbides/nitrides [10,11], and monoelemental 2D materials [12,13] are explored to transcend the limits of graphene. Inversion symmetry breaking and/or introduction of spin-orbit coupling (SOC) to the graphene structure leads to the band gap at the Dirac cone [Fig. 1(a)], which gives massive Dirac fermions [14–20]. Materials with gapped Dirac cones are regarded as promising platforms for valleytronics [21–23], a novel mechanism of electronics. A topological flat band has a contrasting feature that has no energy dispersion in the entire k-space. In contrast to a Dirac cone, the effective mass of the topological flat band can be regarded as infinitely heavy. Structural models for topological flat bands, such as Kagome lattices [Fig. 1(b)] [24,25], Lieb lattices [26–28], etc. [29,30], are being actively investigated, since flat band dispersion has a possibility of providing ferromagnetism [26,31–34] and superconductivity [35,36]. There are a number of theoretical structural models for such topological band structures from the physical point of view [37–42], but it is still difficult to find a suitable chemical structure that realizes the geometry and interactions of ideal model structures. Establishment of a chemical methodology to prepare materials that realize Dirac cones and flat bands is an urgent topic.

In the field of topological physics, inorganic materials used to be the main research focus because of their stronger interaction compared to organic or molecular materials. In recent years, research interest has spread to metal–organic and organic materials [28,43–46]. We focused on molecular freedom for the construction of topological materials. Previously we demonstrated that polyhedral π-conjugated molecules with threefold rotation symmetry (hereafter denoted as polyhedral π-molecules) such as triptycene tri-*p*-benzoquinone (*p*-TT) [47] and naphthalenediimide (NDI)-Δ [48] form highly symmetric 2D (honeycomb) and three-dimensional (3D) (gyroid) crystal structures, and their band structures calculated with tight binding models include both Dirac cones and flat bands [49,50] [Figs. 1(c) and 1(d)]. Highly symmetric and unique arrangements of π-conjugated fragments of polyhedral π-molecules enable the formation of efficiently correlated 2D and 3D network structures by π-π interactions. One of the advantages of organic materials is that the structures, interactions, and redox capacities of molecules can be tuned by chemical modification, which provides a variety of crystal and band structures, and makes it possible to control the band filling. Actually, large numbers of polyhedral π-molecules with various functional groups have been reported so far. Research into these polyhedral π-molecules motivated us to investigate their crystal structures and electronic band structures further.

Here, we propose a rational method to construct a Dirac cone and flat band, and to introduce a mass term to the Dirac Hamiltonian by using organic molecules. We theoretically investigated the band structures of 2D triangular lattices formed by polyhedral π-molecules. Based on the fragment molecular orbital picture, we systematically calculate the band structures of polyhedral π-molecules based triangle lattices and discuss their topological features and the origins of their topological band structures.
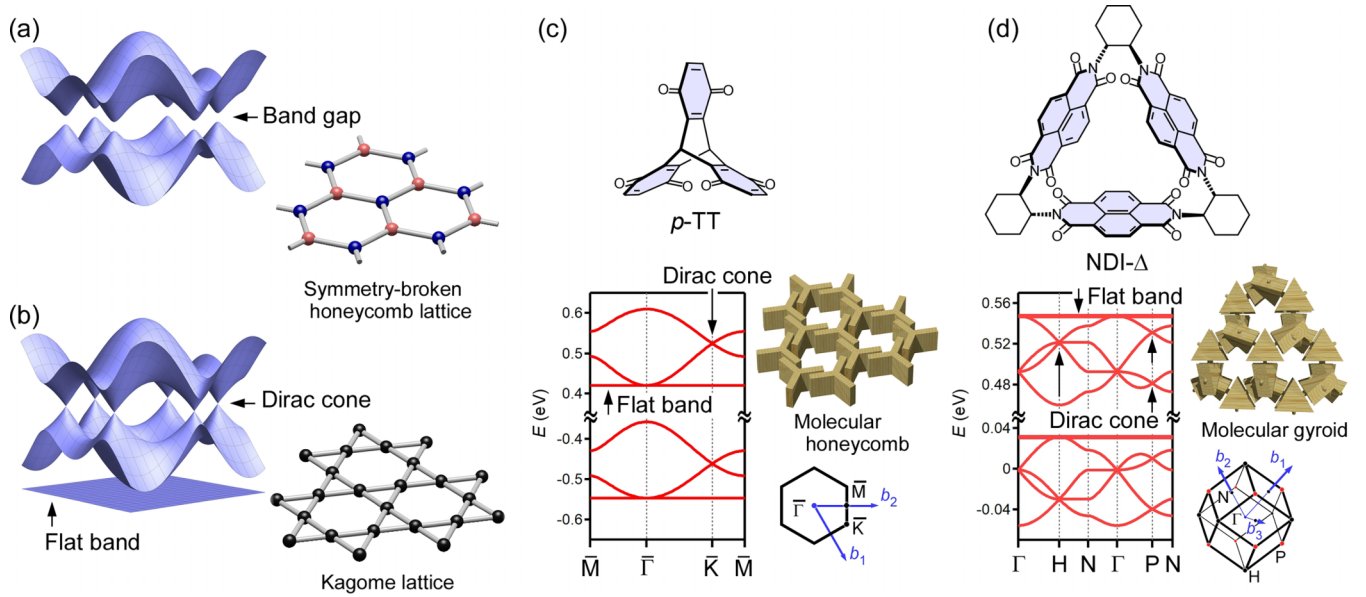
FIG. 1. Topological band structures of the model structures and polyhedral π-conjugated molecules. (a) Gapped Dirac cone of symmetry-broken honeycomb lattice. (b) Coexisting Dirac cone and flat band of kagome lattice. (c) and (d) Molecular structures and schematic images of crystal packings and band structures of polyhedral π-molecules p-TT (c) and NDI-Δ (d). The three π-fragments that consist of molecules are blue.

II. MOLECULAR ORBITALS AND INTRAMOLECULAR INTERACTIONS

The possible shapes of polyhedral π-molecules can be classified into two types, labeled Y and Δ types, in which π-fragments are connected as paddlewheel-like (p-TT) and triangular (NDI-Δ), respectively. In both types of polyhedral π-molecules, the molecular orbitals (MOs), Ψ, can be expressed as linear combinations of frontier MOs of three constituent π-fragments (φ), $|\Psi\rangle = c_A|\varphi_A\rangle + c_B|\varphi_B\rangle + c_C|\varphi_C\rangle$. In this work, we consider only the π-orbitals and their interactions, because the frontier orbitals of such π-fragments are generally π-MOs. The Hamiltonian for the three interacting π-fragments in a molecule (H_{intra}) can be expressed as

$$H_{\text{intra}} = \begin{pmatrix} 0 & -t_0 & -t_0 \\ -t_0 & 0 & -t_0 \\ -t_0 & -t_0 & 0 \end{pmatrix}, \quad (1)$$

where t_0 is the intramolecular transfer integral between π-fragments. The diagonal term shows the Coulomb integral of the π-fragment, which is defined as the origin of the energy.

Based on this Hamiltonian, the energy levels of MOs are given as $E = t_0, t_0, -2t_0$. For each energy level, coefficients of the MO have the following relationships: $c_A + c_B + c_C = 0$ ($E = t_0$) and $c_A = c_B = c_C (E = -2t_0)$. The MOs of a polyhedral π-molecule can be expressed as one-dimensional, $\psi_a \propto (\varphi_A + \varphi_B + \varphi_C)$, and two-dimensional, $\psi_e \propto (\varphi_A - \varphi_B), (\varphi_A + \varphi_B - 2\varphi_C)$, as illustrated in Fig. 2. The energy splitting of MOs represents $3t_0$ and the sign of t_0 can be determined by the positions of degenerate orbitals in energy. The MOs of polyhedral π-molecules and the sign of t_0 can be clearly explained by the schematic MOs and energy diagram. When t_0 is negative, the degenerated orbitals Ψ_e are more stable (bonding) than nondegenerated orbital Ψ_a [Figs. 2(a) and 2(b)]. When t_0 is positive, Ψ_a can be

drawn as all bonding interactions and are more stable than Ψ_e [Fig. 2(c)]. For Y-type molecules, t_0 are negative regardless of the constituent π-orbitals [Fig. 2(a)]. On the other hand, the sign of t_0 for Δ-type molecules can be determined by the number of nodes between the joints of π-fragments—specifically, an odd number of nodes gives $t_0 < 0$ [Fig. 2(b)] and an even number gives $t_0 > 0$ [Fig. 2(c)]. The density functional theory calculations on the reported polyhedral π-molecules were also performed (Sec. I of Supplemental Material [51]). The MOs of Y-type molecules triptycene tri-o-benzoquinone (o-TT) [52] and triptycene trithianthrene (TTA) [53] in Supplemental Material Fig. S2 [51], and Δ-type molecules pyromellitdiimide (PMDI)-Δ [54] and NDI-Δ [48] in Supplemental Material Fig. S3 [51] show the clear correspondence of the MOs and sign of t_0.

III. MOLECULAR PACKINGS AND INTERMOLECULAR INTERACTIONS IN TRIANGULAR LATTICES

The model structures we consider are triangular arrangements of polyhedral π-molecules, which are connected
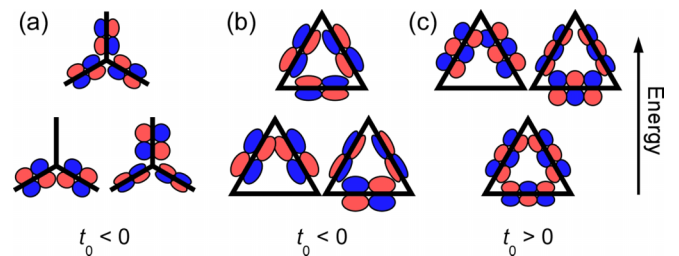

FIG. 2. Schematic images of molecular orbitals and signs of t_0. (a)–(c) The interaction can be categorized as Y-type molecules (a) and Δ-type molecules with odd (b) and even numbers (c) of nodes in π-fragments.
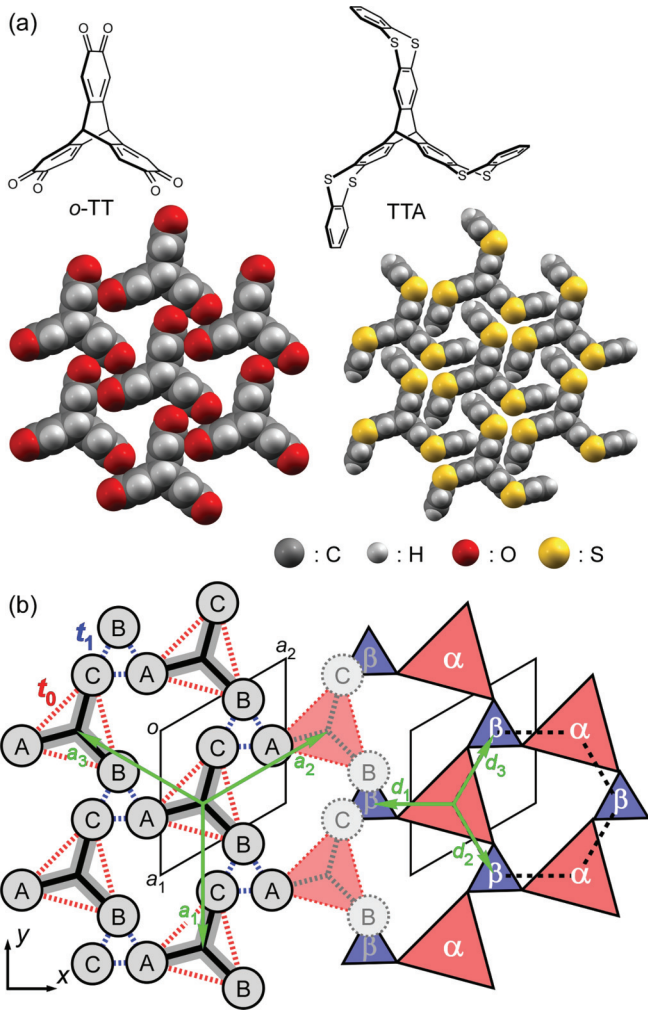
FIG. 3. (a) Representative crystal packing of triangle lattice of Y-type molecules *o*-TT [52] and TTA [53]. The gray, white, red, and yellow spheres show carbon, hydrogen, oxygen, and sulfur atoms, respectively. (b) Schematic packing motif of polyhedral π-molecules. The left side shows the schematic image of t_0 and t_1 interactions between the π-fragments (gray circles with A, B, and C) of polyhedral molecules. The right side shows the hexagonal packing of intra- and intermolecular trimers of π-fragments (red triangles with α and blue triangles with β, respectively), and the vectors between them (d_1, d_2 and d_3).

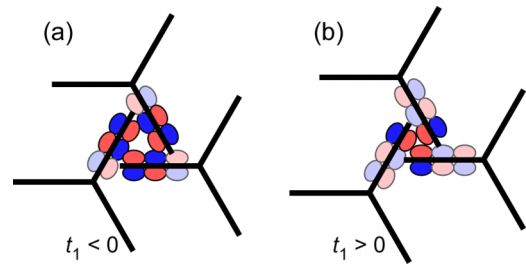FIG. 4. Schematic image of an intermolecular MO overlaps. The sign of t_1 is determined by the overlap symmetry. (a) The case of $t_0 < 0$ with odd number of nodes in a trimer overlap. (b) The case of $t_0 > 0$ with even number of nodes.

π-conjugated fragments of a polyhedral π-molecule are shown as gray circles (labeled A, B, and C) connected by intramolecular interactions (t_0, red dotted lines). One polyhedral molecule interacts with six neighboring molecules in a triangular lattice by t_1 (blue dotted lines). The existent 3D crystal structures might be less symmetric than the ideal triangular lattice, presumably because of interlayer arrangements or the symmetry of crystal solvents. Though the lower symmetry raises small differences in interactions, we approximate that the interactions of the 2D triangular lattice system are symmetric. Here we also ignore the interlayer interactions, because the unique molecular shapes of polyhedral π-molecules enable the intralayer π-π interactions to be much stronger than interlayer interactions.

With this consideration, the Hamiltonian of the nearest-neighboring π-π interactions can be expressed as

$$H_{\text{inter}} = \begin{pmatrix} 0 & -t_1 & -t_1 \\ -t_1 & 0 & -t_1 \\ -t_1 & -t_1 & 0 \end{pmatrix}, \qquad (2)$$

where t_1 is the intermolecular transfer integral. Since the intermolecular trimer of a π-fragment forms a triangular arrangement, as shown in Fig. 4, t_1 can be estimated in the same manner as discussed for the t_0 of Δ-type molecules, and the sign of t_1 is sensitive to the intermolecular overlaps. Although it is difficult to achieve the alternating signs of transfer integrals in inorganic materials, the π-molecules with clearly determined positive and negative transfer integrals have an advantage for the $t_0/t_1 < 0$ system.

IV. BAND STRUCTURE CALCULATIONS IN RECIPROCAL SPACE

We constructed a tight binding model of polyhedral π-molecules in a triangular lattice with t_0 and t_1. Since there are three sites of π-fragments (A, B, and C) in the unit cell, the Hamiltonian can be described by a 3×3 matrix:

to each other by intermolecular π-π interactions. This arrangement is observed in, for example, neutral triptycene derivatives *o*-TT [52] and TTA [53], which consist of three *o*-benzoquinone and thianthrene moieties, respectively [Fig. 3(a)]. Based on the existent crystal structures, we constructed a model structure of a polyhedral π-molecule–based triangular lattice, as shown in Fig. 3(b), left. Three

$$H_{\text{cryst}}(k) = \begin{pmatrix} 0 & -t_0 e^{ik \cdot R_{\text{AB}}} - t_1 e^{ik \cdot R'_{\text{AB}}} & -t_0 e^{ik \cdot R_{\text{AC}}} - t_1 e^{ik \cdot R'_{\text{AC}}} \\ -t_0 e^{ik \cdot R_{\text{BA}}} - t_1 e^{ik \cdot R'_{\text{BA}}} & 0 & -t_0 e^{ik \cdot R_{\text{BC}}} - t_1 e^{ik \cdot R'_{\text{BC}}} \\ -t_0 e^{ik \cdot R_{\text{CA}}} - t_1 e^{ik \cdot R'_{\text{CA}}} & -t_0 e^{ik \cdot R_{\text{CB}}} - t_1 e^{ik \cdot R'_{\text{CB}}} & 0 \end{pmatrix}, \qquad (3)$$

where R_{AB} and R'_{AB} represent the vectors connecting the centers of the nearest-neighboring fragments within the molecule and between the molecules, respectively (see Sec. II of Supplemental Material [51]). As discussed earlier, the absolute values and signs of t_0 and t_1 can be determined by the molecular shapes, MOs of π-fragments, and intermolecular overlaps in their crystal structures, and can be regarded as independent parameters for model calculation. As an example of an existent system, the MOs and energy diagrams of Y-type π-molecules o-TT and TTA are shown in Supplemental Fig. S2 [51], and their transfer integrals can be estimated as $t_0 = -0.26$ eV and $t_1 = -0.093$ eV for o-TT, and $t_0 = -0.067$ eV and $t_1 = +0.12$ eV for TTA. To interpret the nature of their band structures, we constructed tight binding models by systematically changing the parameters t_0 and t_1. Figures 5(a) and 5(b) show the calculated band structures of polyhedral π-molecules in a triangular lattice with some selected parameters. For better visibility, the energy was normalized by $|t_0 + t_1|$ for $t_0/t_1 > 0$ [Fig. 5(a)] and $|t_0 - t_1|$ for $t_0/t_1 < 0$ [Fig. 5(b)]. As a general feature of the band structures, the same energy (E) is obtained by swapping t_0 and t_1, and energy with the opposite sign ($-E$) is obtained by reversing both signs of t_0 and t_1. Hereafter we show the band structures of $t_1 < t_0 < 0$ for $t_0/t_1 > 0$ and $-t_1 < t_0 < 0$ for $t_0/t_1 < 0$. Regardless of the conditions of t_0 and t_1, a flat band was always observed. Conical dispersions with single-point band touching were also observed in some critical conditions, specifically when $t_1/t_0 = 1$ at the $\bar{K}$-point and when $t_1/t_0 = -1$ at the $\bar{\Gamma}$-point, and the difference between $|t_0|$ and $|t_1|$ brings band gaps on these points.

The topological features of the flat band and the point nodes become apparent by tracking the singularity of the wavefunction. For this purpose, we analyze the Berry curvature, $\Omega_\nu(k) \equiv \frac{\partial}{\partial k_x} A_\nu^y(k) - \frac{\partial}{\partial k_y} A_\nu^x(k)$, where ν is the band index and $A_\nu(k) = (A_\nu^x(k), A_\nu^y(k))$ is the so-called Berry connection $A_\nu(k) \equiv -i\langle \Psi_\nu(k)|\nabla_k|\Psi_\nu(k)\rangle$, representing how the wave function varies by k [55–59]. For several choices of parameters, $\Omega_\nu(k)$ are projected onto the band structure as shown in Figs. 5(e)–5(h). The $\Omega_\nu(k)$ values of the respective bands are shown in Figs. 5(i)–5(l). In the case of a regular kagome lattice, $\Omega_\nu(k)$ becomes zero except for the Dirac points. In the present case, $\Omega_\nu(k)$ becomes nonzero at general points of k, since the inversion symmetry is broken due to the imbalance between hopping amplitudes t_0 and t_1, and due to the deviation of the positions of the center of mass from the kagome sites. The net topology of each band can be characterized by the Chern number $C_\nu \equiv \frac{1}{2\pi} \int_{BZ} \Omega_\nu(k) d^2k$, where the integral over k is taken in the first Brillouin zone. As seen from Figs. 5(e) and 5(i), $\Omega_\nu(k)$ has an opposite sign by $k \rightarrow -k$, and thus the Chern number of each band is zero, indicating it is topologically trivial.

However, the situation can be altered by introducing infinitesimal SOC [60]. Here we analyze the Berry curvature in the presence of the weak intrinsic SOC. As is well known for the honeycomb lattice, the topological phase transition arises from the competition between the inversion symmetry breaking and the spin–orbit coupling [58]. In our polyhedral π-molecule system, the three bands show small spin splitting when the weak, intrinsic SOC is introduced, as shown in

Supplemental Material Figs. S6 and S7 [51]. The profile of the Berry curvature near the Dirac points $\bar{K}$ and $\overline{K'}$ shown in Figs. 5(g) and 5(j) are essentially the same as in the case without SOC, since the inversion symmetry-breaking effect dominates the SOC effect. On the other hand, $\Omega_\nu(k)$ for the flat band has a significant amplitude near the $\bar{\Gamma}$-point. Since the spin-splitting bands have opposite signs of Berry curvature, the spin Chern number of the flat band becomes ± 1. The flat band has no characteristic energy scale, and thus the infinitesimal SOC can make the flat band topological. In addition, the dispersive middle band also acquires a nonzero spin-Chern number with the opposite sign, as seen in Figs. 5(g) and 5(j). A similar feature is observed at the $\bar{\Gamma}$-point of $t_0/t_1 < 0$ in Figs. 5(h) and 5(l). The spin-Chern number for each band can be controlled by the systematic change in the hopping amplitudes. The topological flat band and the dispersive bands made by the polyhedral π-molecule thus have a potential application to a new type of valleytronics device [21–23], the emerging spin Hall effect [16,17,38], and other topology-related phenomena [55–58]. The nonzero spin-Chern number is directly related to the singular behavior of the spin Hall effect, by the so-called Thouless-Kohmoto-Nightingale-Nijs formula [61,62]. The calculated spin Hall conductivity σ_{xy}^{spin} is shown in Figs. 5(c) and 5(d). As the Fermi energy approaches the energy level of the flat band, the spin Hall conductivity is significantly enhanced and reaches the universal value $e/2\pi$. To realize the physical properties based on the topological band structure, band width and band filling are important factors. The estimated band widths from the crystal structures are 1 eV for o-TT and 0.6 eV for TTA, which are sufficient dispersions for physical property measurements. The valence/conduction band of the neutral o-TT and TTA are fully occupied/empty, but the electron accepting/donating ability of o-TT/TTA enables up to three electron reductions/oxidations [52,53]. These redox abilities cover the filling control of one and a half bands, and are accessible to the topological bands of triangular lattices.

V. ORIGIN OF THE TOPOLOGICAL FLAT BAND AND THE EFFECTIVE LOW-ENERGY THEORY FOR DIRAC AND NON-DIRAC POINT NODES

The topological flat band originates from the interference effect of wavefunctions due to the C_3 symmetry of the molecular structure and the triangular lattice. Moreover, the emergence of the topological flat band indicates that the macroscopic number of the wavefunctions localized in real space have a common energy. In the following, the origin of the topological flat band is clarified by building the localized wavefunction explicitly. In terms of the localized Wannier orbital of the π-fragment $|\varphi_{A,B,C}(R)\rangle$, the wavefunction of the system can be expressed as

$$|\Psi\rangle = \sum_n \left[c_A(R_n^A)|\varphi_A(R_n^A)\rangle + c_B(R_n^B)|\varphi_B(R_n^B)\rangle \right.$$
$$\left. + c_C(R_n^C)|\varphi_C(R_n^C)\rangle \right], \qquad (4)$$

where $c_{A,B,C}$ are the coefficients to be determined to satisfy the Schrödinger equation, $R_n^{A,B,C}$ indicate the position of the center of mass of the fragment, and n is the index of the unit
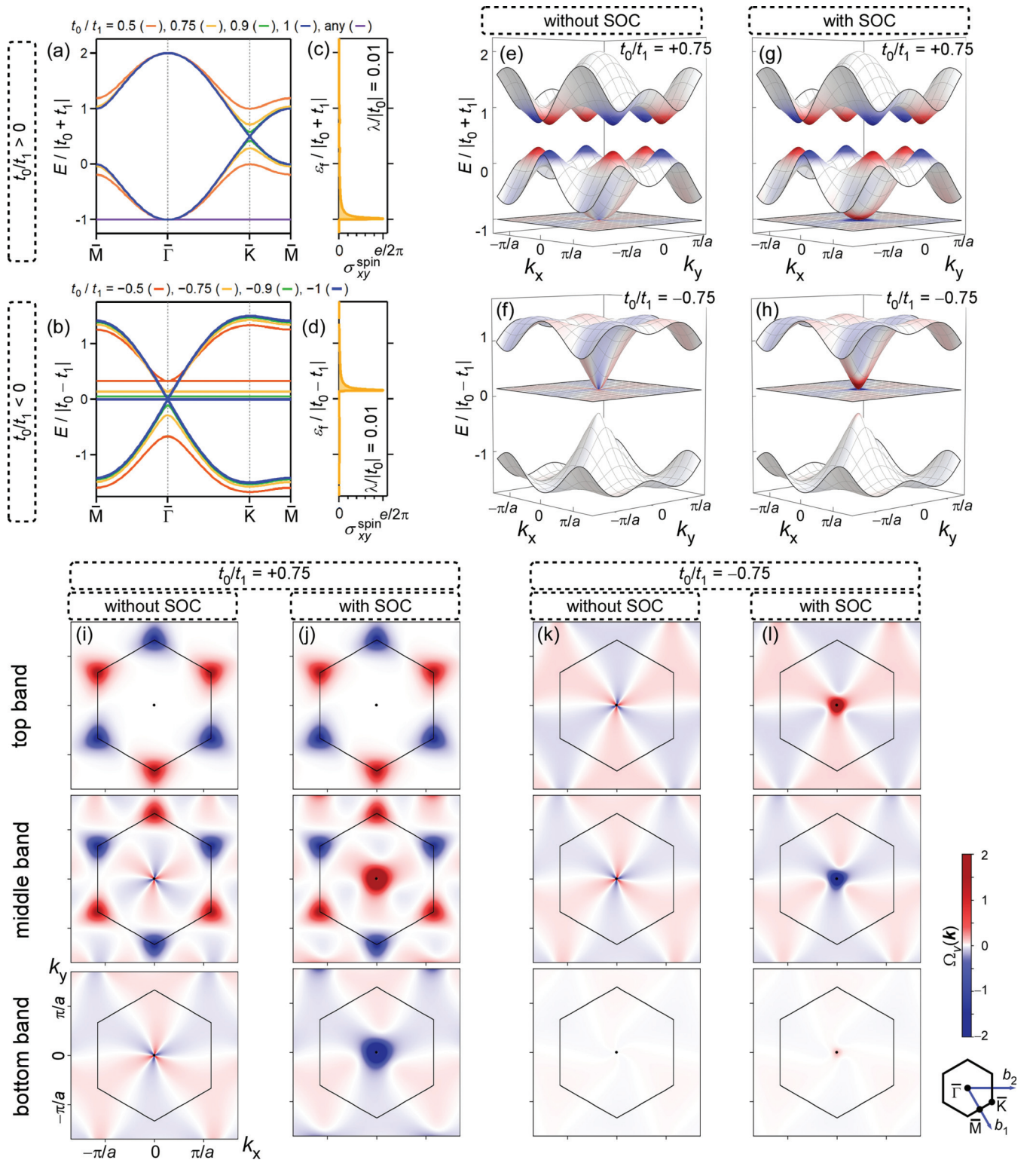
FIG. 5. Electronic band structures and Berry curvatures of polyhedral π-molecules in triangular lattices. (a)–(d) Calculated band structures with variable t_0/t_1 values, the signs of which are positive (a) and negative (b), and their spin Hall conductivity [(c) and (d)]. (e)–(h) 3D plots of the band structures for $t_0/t_1 = +0.75$ [(e) and (g)] and -0.75 [(f) and (h)] with the color scale of Berry curvature without [(e) and (f)] and with SOC [(g) and (h)]. (i)–(l) Berry curvature of each band. The signs of t_0 and t_1 were set as $t_0 < 0$ and $t_1 < 0$ for $t_0/t_1 > 0$, and $t_0 < 0$ and $t_1 > 0$ for $t_0/t_1 < 0$.
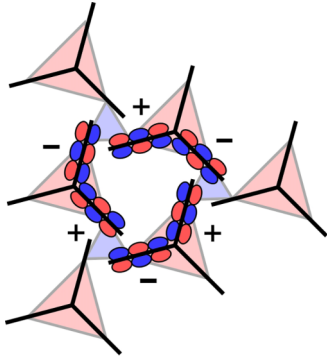
FIG. 6. Localized wavefunction that forms a topological flat band. The signs $+$ and $-$ represent the coefficients of π-fragments. The coefficient of the π-fragment is zero when the MO is not shown.

cell. If we consider an isolated molecule with C_3 symmetry, where the Hamiltonian is given in Eq. (1), doubly degenerate e-orbitals are constructed by the orthogonality condition to the one-dimensional a-orbital, i.e., $c_A + c_B + c_C = 0$. In the case of the crystal shown in Fig. 3, the system has another C_3 symmetry reflecting the triangular lattice structure, as seen in Eq. (2). These two kinds of C_3 symmetry give rise to the emergence of the macroscopically degenerate state, i.e., the topological flat band. The degeneracy within the intramolecular π-trimer [shown by red triangles in Fig. 3(b), right] can be analyzed by the quantity

$$\alpha\left(R_n^\alpha\right) \equiv c_A\left(R_n^A\right) + c_B\left(R_n^B\right) + c_C\left(R_n^C\right), \qquad (5)$$

where we introduce the index α, indicating the center of mass of the π-trimer, and R_n^α represents its position. The degenerate MOs can be constructed by $\alpha(R_n^\alpha) = 0$. Next, the degeneracy within the intermolecular π-trimer [shown by blue triangles in Fig. 3(b), right] can be analyzed by the quantity

$$\beta\left(R_n^\beta\right) \equiv c_A\left(R_n^A + a_2\right) + c_B\left(R_n^B - a_1\right) + c_C\left(R_n^C\right), \quad (6)$$

where the index β represents the center of mass of the intermolecular π-trimer and its position is given by R_n^β. The localized molecular orbitals with macroscopic degeneracy can be constructed from the condition $\alpha(R_n^\alpha) = \beta(R_n^\beta) = 0$ for any site **n**. This condition can be fulfilled by imposing $(c_A, c_B, c_C) \propto (+1, -1, 0)$, $(0, +1, -1)$, or $(-1, 0, +1)$ for sites inside the localized orbital and $(c_A, c_B, c_C) = (0, 0, 0)$ for sites outside. A wavefunction constructed in this manner is illustrated in Fig. 6, where the sum of coefficients in all intra- and intermolecular trimers is canceled out to zero. The energy of this localized state is $E_{flat} = t_0 + t_1$ (Sec. III of Supplemental Materials [51]). Since the position of the localized state is arbitrary, the bulk number of such localized states degenerates, and thus the flat band emerges in the polyhedral π-molecule -based triangular lattice.

To investigate the nature of the remaining two dispersive bands, especially of the point nodes at the $\bar{K}$-, $\bar{K}'$-, and $\bar{\Gamma}$-points, we derive a 2×2 Hamiltonian matrix and analyze its low-energy structure. The wavefunction coefficients of the dispersive bands satisfy $\alpha(R_n^\alpha) \neq 0$ and $\beta(R_n^\beta) \neq 0$. The coefficients α and β can be determined by solving the eigenvalue problem of the 2×2 matrix (Sec. III of Supplemental

Material [51]):

$$E_k'\begin{pmatrix} \tilde{\alpha}_k \\ \tilde{\beta}_k \end{pmatrix} = H_k\begin{pmatrix} \tilde{\alpha}_k \\ \tilde{\beta}_k \end{pmatrix},$$

$$H_k = \begin{pmatrix} -\frac{3}{2}(t_0 - t_1) & \sqrt{|t_0 t_1|}\frac{a}{\hbar}\gamma_k \\ \sqrt{|t_0 t_1|}\mathrm{sgn}(t_0 t_1)\frac{a}{\hbar}\gamma_k^* & +\frac{3}{2}(t_0 - t_1) \end{pmatrix}, \qquad (7)$$

where $\tilde{\alpha}_k$ and $\tilde{\beta}_k$ are the Bloch wave functions built up by $\alpha(R_n^\alpha)$ and $\beta(R_n^\beta)$, respectively. Here, $E_k' \equiv E_k + (t_0 + t_1)/2$ and $\gamma_k \equiv i\hbar(e^{ik\cdot d_1} + e^{ik\cdot d_2} + e^{ik\cdot d_3})/a$. The diagonal energy of H_k is shifted to make it traceless. The matrix H_k has different properties depending on the sign of t_0/t_1. In the following, we discuss the low-energy effective Hamiltonian separately.

In the case of $t_0/t_1 > 0$, the gap between the two bands becomes small at the $\bar{K}$- and $\bar{K}'$-points. By setting $k = K + q$ or $k = K' + q$, and by assuming small $|q|$, Eq. (7) can be expressed by the well-known two-dimensional massive Dirac Hamiltonian

$$H_{K+q} = v\hbar q_x \sigma_x + \tau_z v\hbar q_y \sigma_y + mv^2 \sigma_z, \qquad (8)$$

where $\sigma_{x,y,z}$ are the Pauli matrices. The velocity and the mass are given by $v \equiv (\sqrt{3}a/2\hbar)\sqrt{|t_0 t_1|}$ and $m \equiv -(2\hbar^2/a^2)(t_0 - t_1)/|t_0 t_1|$. Here, τ_z represents the valley degree of freedom: $\tau_z = +1$ for the $\bar{K}$-point and $\tau_z = -1$ for the $\bar{K}'$-point. This result indicates that the $\bar{K}$- and $\bar{K}'$-points have opposite chirality, as can also be seen from the profile of the Berry curvature shown in Fig. 5(g). Equation (8) has the energy eigenvalue

$$E_k' = \pm\sqrt{v^2\hbar^2 q^2 + m^2 v^4}, \qquad (9)$$

which indicates the massive ($m \neq 0$) and massless ($m = 0$) Dirac cones. The lattice geometry in the case of $t_0/t_1 > 0$ is the same as that of the so-called breathing kagome lattice [37,39], and the effective theory [Eq. (8)] has the same structure observed in the honeycomb lattice with chiral symmetry breaking [14,17–20]. It is worth noting that R_n^α and R_n^β introduced in Eqs. (5) and (6) form two sublattice vectors of the honeycomb lattice, and the asymmetry between the intra- and intermolecular trimers causes the effect of chiral symmetry breaking the honeycomb lattice, i.e., the nonzero mass term of the Dirac Hamiltonian.

In the case of $t_0/t_1 < 0$, the gap becomes small at the $\bar{\Gamma}$-point. By assuming small $k = \sqrt{k_x^2 + k_y^2}$, the matrix H_k can be described by

$$H_k = \begin{pmatrix} -\frac{3}{2}(t_0 - t_1) & i\sqrt{|t_0 t_1|}\left(3 - \frac{1}{4}k^2 a^2\right) \\ i\sqrt{|t_0 t_1|}\left(3 - \frac{1}{4}k^2 a^2\right) & +\frac{3}{2}(t_0 - t_1) \end{pmatrix}, \quad (10)$$

and its eigenenergy is given by

$$E_k' = \pm\sqrt{\frac{9}{4}(t_0 + t_1)^2 + \frac{3}{2}|t_0 t_1|k^2 a^2}. \qquad (11)$$

The gap amplitude at the $\bar{\Gamma}$-point is $3|t_0 + t_1|$. If $(t_0 + t_1) = 0$, two bands degenerate at $k = 0$ and exhibit linear k dependence, $E_k' \propto \pm\sqrt{k_x^2 + k_y^2}$. This conical band behavior cannot be attributed to the Dirac dispersion since no peculiar signature can be observed in the Berry curvature [Figs. 5(f) and 5(k)].

VI. CONCLUSION

In summary, we proposed that the molecular freedom of polyhedral π-molecules with threefold rotation symmetry can provide a rational method of constructing topological band structures. The independently controllable interactions t_0 and t_1 provide massless/massive Dirac cones and topological flat bands. The difference between t_0 and t_1 leads to a band gap opening and nonzero Berry curvature on the Dirac cone. Additionally, infinitesimal SOC gives a nontrivial Chern number on the topological flat band. The topological flat band can be attributed to the interference effect of wavefunctions due to the C_3 symmetry of the molecule and lattice. The Dirac cone originates from the honeycomb arrangement of π-fragment trimers, and the mass term is given by the difference between t_0 and t_1, which breaks the inversion symmetry of the honeycomb structure.

[1] P. R. Wallace, The band theory of graphite, Phys. Rev. **71**, 622 (1947).

[2] A. H. Castro Neto, F. Guinea, N. M. R. Peres, K. S. Novoselov, and A. K. Geim, The electronic properties of graphene, Rev. Mod. Phys. **81**, 109 (2009).

[3] N. O. Weiss, H. Zhou, L. Liao, Y. Liu, S. Jiang, Y. Huang, and X. Duan, Graphene: An emerging electronic material, Adv. Mater. **24**, 5782 (2012).

[4] K. S. Novoselov, A. K. Geim, S. V. Morozov, D. Jiang, M. I. Katsnelson, I. V. Grigorieva, S. V. Dubonos, and A. A. Firsov, Two-dimensional gas of massless Dirac fermions in graphene, Nature (London) **438**, 197 (2005).

[5] Q. Tang and Z. Zhou, Graphene-analogous low-dimensional materials, Prog. Mater. Sci. **58**, 1244 (2013).

[6] G. R. Bhimanapati *et al.*, Recent advances in two-dimensional materials beyond graphene, ACS Nano **9**, 11509 (2015).

[7] R. Roldán, L. Chirolli, E. Prada, J. A. Silva-Guillén, P. San-Jose, and F. Guinea, Theory of 2D crystals: Graphene and beyond, Chem. Soc. Rev. **46**, 4387 (2017).

[8] Q. H. Wang, K. Kalantar-Zadeh, A. Kis, J. N. Coleman, and M. S. Strano, Electronics and optoelectronics of two-dimensional transition metal dichalcogenides, Nat. Nanotechnol. **7**, 699 (2012).

[9] M. Chhowalla, H. S. Shin, G. Eda, L.- J. Li, K. P. Loh, and H. Zhang, The chemistry of two-dimensional layered transition metal dichalcogenide nanosheets, Nat. Chem. **5**, 263 (2013).

[10] M. Naguib, V. N. Mochalin, M. W. Barsoum, and Y. Gogotsi, 25th Anniversary article: MXenes: A new family of two-dimensional materials, Adv. Mater. **26**, 992 (2014).

[11] M. Khazaei, A. Ranjbar, M. Arai, T. Sasaki, and S. Yunoki, Electronic properties and applications of MXenes: A theoretical review, J. Mater. Chem. C **5**, 2488 (2017).

[12] M. Pumera and Z. Sofer, 2D Monoelemental arsenene, antimonene, and bismuthene: Beyond black phosphorus, Adv. Mater. **29**, 1605299 (2017).

[13] N. R. Glavin, R. Rao, V. Varshney, E. Bianco, A. Apte, A. Roy, E. Ringe, and P. M. Ajayan, Emerging applications of elemental 2D materials, Adv. Mater. **32**, 1904302 (2020).

[14] D. Xiao, W. Yao, and Q. Niu, Valley-Contrasting Physics in Graphene: Magnetic Moment and Topological Transport, Phys. Rev. Lett. **99**, 236809 (2007).

[15] S. Konschuh, M. Gmitra, and J. Fabian, Tight-binding theory of the spin-orbit coupling in graphene, Phys. Rev. B **82**, 245412 (2010).

[16] C.- C. Liu, W. Feng, and Y. Yao, Quantum Spin Hall Effect in Silicene and Two-Dimensional Germanium, Phys. Rev. Lett. **107**, 076802 (2011).

[17] D. Xiao, G.- B. Liu, W. Feng, X. Xu, and W. Yao, Coupled Spin and Valley Physics in Monolayers of MoS$_2$ and other Group-VI Dichalcogenides, Phys. Rev. Lett. **108**, 196802 (2012).

[18] N. D. Drummond, V. Zolyomi, and V. I. Fal'ko, Electrically tunable band gap in silicene, Phys. Rev. B **85**, 075423 (2012).

[19] J. Wang, S. Deng, Z. Liu, and Z. Liu, The rare two-dimensional materials with Dirac cones, Natl. Sci. Rev. **2**, 22 (2015).

[20] E. Wang, X. Lu, S. Ding, W. Yao, M. Yan, G. Wan, K. Deng, S. Wang, G. Chen, L. Ma, J. Jung, A. V. Fedorov, Y. Zhang, G. Zhang, and S. Zhou, Gaps induced by inversion symmetry breaking and second-generation Dirac cones in graphene/hexagonal boron nitride, Nat. Phys. **12**, 1111 (2016).

[21] J. R. Schaibley, H. Yu, G. Clark, P. Riveral, J. S. Ross, K. L. Seyler, W. Yao, and X. Xu, Valleytronics in 2D materials, Nat. Rev. Mater. **1**, 16055 (2016).

[22] S. Li, J. He, L. Grajciar, and P. Nachtigall, Intrinsic valley polarization in 2D magnetic MXenes: Surface engineering induced spin-valley coupling, J. Mater. Chem. C **9**, 11132 (2021).

[23] S. Zhao, X. Li, B. Dong, H. Wang, H. Wang, Y. Zhang, Z. Han, and H. Zhang, Valley manipulation in monolayer transition metal dichalcogenides and their hybrid systems: Status and challenges, Rep. Prog. Phys. **84**, 026401 (2021).

[24] A. Mielke, Exact ground states for the Hubbard model on the kagome lattice, J. Phys. A Math. Gen. **25**, 4335 (1992).

[25] M. Kang, S. Fang, L. Ye, H. C. Po, J. Denlinger, C. Jozwiak, A. Bostwick, E. Rotenberg, E. Kaxiras, J. G. Checkelsky, and R. Comin, Topological flat bands in frustrated kagome lattice CoSn, Nat. Commun. **11**, 4004 (2020).

[26] E. H. Lieb, Two theorems on the Hubbard model, Phys. Rev. Lett. **62**, 1201 (1989).

[27] C. Weeks and M. Franz, Topological insulators on the Lieb and perovskite lattices, Phys. Rev. B **82**, 085310 (2010).

[28] B. Cui, X. Zheng, J. Wang, D. Liu, S. Xie, and B. Huang, Realization of Lieb lattice in covalent-organic frameworks with tunable topology and magnetism, Nat. Commun. **11**, 66 (2020).

[29] T. Mizoguchi, H. Katsura, I. Maruyama, and Y. Hatsugai, Flat-band solutions in D-dimensional decorated diamond and pyrochlore lattices: Reduction to molecular problem, Phys. Rev. B **104**, 035155 (2021).

[30] C. S. Chiu, A. N. Carroll, N. Regnault, and A. A. Houck, Line-graph-lattice crystal structures of stoichiometric materials, Phys. Rev. Res. **4**, 023063 (2022).

[31] A. Mielke, Ferromagnetism in the Hubbard model on line graphs and further considerations, J. Phys. A Math. Gen. **24**, 3311 (1991).

[32] H. Tasaki, Ferromagnetism in the Hubbard Models with Degenerate Single-Electron Ground States, Phys. Rev. Lett. **69**, 1608 (1992).

[33] A. Mielke and H. Tasaki, Ferromagnetism in the Hubbard model, Commun. Math. Phys. **158**, 341 (1993).

[34] K. Ohgushi, S. Murakami, and N. Nagaosa, Spin anisotropy and quantum Hall effect in the kagome lattice: Chiral spin state based on a ferromagnet, Phys. Rev. B **62**, R6065 (2000).

[35] H. Aoki, Theoretical possibilities for flat band superconductivity, J. Supercond. Nov. Magn. **33**, 2341 (2020).

[36] K. Kobayashi, M. Okumura, S. Yamada, M. Machida, and H. Aoki, Superconductivity in repulsively interacting fermions on a diamond chain: Flat-band-induced pairing, Phys. Rev. B **94**, 214501 (2016).

[37] M. Ezawa, Higher-Order Topological Insulators and Semimetals on the Breathing Kagome and Pyrochlore Lattices, Phys. Rev. Lett. **120**, 026801 (2018).

[38] F. C. de Lima, G. J. Ferreira, and R. H. Miwa, Topological flat band, Dirac fermions and quantum spin Hall phase in 2D Archimedean lattices, Phys. Chem. Chem. Phys. **21**, 22344 (2019).

[39] A. Bolens and N. Nagaosa, Topological states on the breathing kagome lattice, Phys. Rev. B **99**, 165141 (2019).

[40] J.- W. Rhim and B.- J. Yang, Classification of flat bands according to the band-crossing singularity of Bloch wave functions, Phys. Rev. B **99**, 045107 (2019).

[41] H. Liu, S. Meng, and F. Liu, Screening two-dimensional materials with topological flat bands, Phys. Rev. Mater. **5**, 084203 (2021).

[42] D. Călugăru, A. Chew, L. Elcoro, Y. Xu, N. Regnault, Z.- D. Song, and B. A. Bernevig, General construction and topological classification of crystalline flat bands, Nat. Phys. **18**, 185 (2022).

[43] W. Jiang, X. Ni, and F. Liu, Exotic topological bands and quantum states in metal–organic and covalent–organic frameworks, Acc. Chem. Res. **54**, 416 (2021).

[44] C. Barreteau, F. Ducastelle, and T. Mallah, A bird's eye view on the flat and conic band world of the honeycomb and Kagome lattices: Towards an understanding of 2D metal-organic frameworks electronic structure, J. Phys. Condens. Matter **29**, 465302 (2017).

[45] S. Baidya, S. Kang, C. H. Kim, and J. Yu, Chern insulator with a nearly flat band in the metal-organic framework-based Kagome lattice, Sci. Rep. **9**, 13807 (2019).

[46] X. Ni, H. Li, F. Liub, and J.- L. Brédas, Engineering of flat bands and Dirac bands in two-dimensional covalent organic frameworks (COFs): Relationships among molecular orbital symmetry, lattice symmetry, and electronic-structure characteristics, Mater. Horiz. **9**, 88 (2022).

[47] G. A. Russell, N. K. Suleman, H. Iwamura, and O. W. Webster, Radical anions of triptycene bis- and tris(quinones), J. Am. Chem. Soc. **103**, 1560 (1981).

[48] S. T. Schneebeli, M. Frasconi, Z. Liu, Y. Wu, D. M. Gardner, N. L. Strutt, C. Cheng, R. Carmieli, M. R. Wasielewski, and J. F. Stoddart, Electron sharing and anion–π recognition in molecular triangular prisms, Angew. Chem. Int. Ed. **52**, 13100 (2013).

[49] Y. Shuku, A. Mizuno, R. Ushiroguchi, C. S. Hyun, Y. J. Ryu, B.- K. An, J. E. Kwon, S. Y. Park, M. Tsuchiizu, and K. Awaga, An exotic band structure of a supramolecular honeycomb lattice formed by a pancake π–π interaction between triradical trianions of triptycene tribenzoquinone, ChemComm **54**, 3815 (2018).

[50] A. Mizuno, Y. Shuku, R. Suizu, M. M. Matsushita, M. Tsuchiizu, D. R. Mañeru, F. Illas, V. Robert, and K. Awaga, Discovery of the K4 structure formed by a triangular π radical anion, J. Am. Chem. Soc. **137**, 7612 (2015).

[51] See Supplemental Material at http://link.aps.org/supplemental/10.1103/PhysRevB.107.155123 for crystal packings, MO diagrams, and detailed expressions for calculations.

[52] S. Langis-Barsetti, T. Maris, and J. D. Wuest, Triptycene 1,2-quinones and quinols: Permeable crystalline redox- active molecular solids, J. Org. Chem. **83**, 15426 (2018).

[53] S. Tang, H. Ruan, Z. Hu, Y. Zhao, Y. Song, and X. Wang, A cationic sulfur-hydrocarbon triradical with an excited quartet state, ChemComm **58**, 1986 (2022).

[54] J. Gawroński, M. Brzostowska, K. Gawrońska, J. Koput, U. Rychlewska, P. Skowronek, and B. Nordén, Novel chiral pyromellitdiimide (1,2,4,5-benzenetetracarboxydiimide) dimers and trimers: Exploring their structure, electronic transitions, and exciton coupling, Chem. Eur. J. **8**, 2484 (2002).

[55] M. Z. Hasan and C. L. Kane, Colloquium: Topological insulators, Rev. Mod. Phys. **82**, 3045 (2010).

[56] D. Xiao, M.- C. Chang, and Q. Niu, Berry phase effects on electronic properties, Rev. Mod. Phys. **82**, 1959 (2010).

[57] X.- L. Qi and S.- C. Zhang, Topological insulators and superconductors, Rev. Mod. Phys. **83**, 1057 (2011).

[58] S.- Q. Shen, Topological Insulators, *Springer Series in Solid-State Sciences 174* (Springer, Heidelberg, 2012).

[59] C. J. Bradley and A. P. Cracknell, *The Mathematical Theory of Symmetry in Solids* (Clarendon Press, Oxford, 1972).

[60] C. L. Kane and E. J. Mele, Quantum Spin Hall Effect in Graphene, Phys. Rev. Lett. **95**, 226801 (2005).

[61] D. J. Thouless, M. Kohmoto, M. P. Nightingale, and M. den Nijs, Quantized Hall Conductance in a Two-Dimensional Periodic Potential, Phys. Rev. Lett. **49**, 405 (1982).

[62] F. D. M. Haldane, Model for a Quantum Hall Effect without Landau Levels: Condensed-Matter Realization of the Parity Anomaly, Phys. Rev. Lett. **61**, 2015 (1988).